Water Research 268 (2025) 122665

Contents lists available at ScienceDirect

Water Research

journal homepage: www.elsevier.com/locate/watres

Selective single-atom adsorption for precision separation of lead ions in tap water *via* capacitive deionization

Zhenwei Gao [a,b], Luqing Wang [a,c], Xingkang Huang [a,b], Chris Benmore [d], Haihui Pu [a,b], Jianguo Wen [c], Wen Zhuang [a,b], Maria K.Y. Chan [c], Junhong Chen [a,b,*]

[a] Pritzker School of Molecular Engineering, University of Chicago, Chicago, Illinois, 60637, United States
[b] Chemical Sciences and Engineering Division, Physical Sciences and Engineering Directorate, Argonne National Laboratory, Lemont, Illinois, 60439, United States
[c] Center for Nanoscale Materials, Argonne National Laboratory, Lemont, Illinois, 60439, United States
[d] Advanced Photon Source, Argonne National Laboratory, Lemont, Illinois, 60439, United States

ARTICLE INFO

Keywords:
Capacitive deionization
Lead removal
Functionalized graphene oxide
Water remediation
Computational modeling

ABSTRACT

Capacitive deionization (CDI) offers a cost-effective and low-energy method for selective removal of Pb^{2+} from drinking water. Modifying CDI electrode surfaces with functional groups presents a versatile approach to enhancing selective ion adsorption capacity. However, a comprehensive understanding of the selectivity and removal efficiency of Pb^{2+} among diverse functional groups remains unexplored. Here, we investigated the effects of different functional groups (-SH, -COOH, and $-NH_2$) attached to the graphene oxide (GO) electrode surfaces on Pb^{2+} selectivity and removal efficiency. Surprisingly, GO-COOH demonstrated single-atom adsorption of Pb^{2+}, displaying superior removal efficiency and selectivity compared with -SH and $-NH_2$, although -SH possesses significant chelation capability for Pb^{2+}. Both density functional theory (DFT) calculations and X-ray pair distribution function (PDF) analyses confirmed that Pb^{2+} exhibits a theoretically higher affinity to -COOH. This research deepens our understanding of the interactions between functional groups and heavy metal ions, enabling selective and rapid separation of target cations for water purification.

1. Introduction

Freshwater scarcity and heavy metal contamination have become major threats to the environment and human health (He et al. 2021, Wei et al. 2023). To protect human health, it is crucial to completely remove minute amounts of hazardous heavy metals like lead ions (Pb^{2+}) from drinking water, because it is one of the most toxic metals that are widely employed in a variety of industrial processes and water pipelines (Arbabi et al. 2015). Pb^{2+} is harmful to human health even at low levels of exposure (Navas-Acien et al. 2007). Therefore, the U.S. Environmental Protection Agency (EPA) has set its maximum contaminant level (MCL) goal and action level at zero and 15 ppb, respectively, in drinking water (EPA 2022). On the other hand, healthy cations in drinking water, such as Ca^{2+} and Mg^{2+} do not need to be fully eliminated because they are beneficial to human health in reasonable amounts, as recommended by the World Health Organization (WHO 2005). Thus, precision separation of trace amounts of heavy metals in various water sources is critical to enabling water reuse and resource recovery.

A current grand challenge is the efficient, cost-effective, and selective separation of various species in water at low concentrations. Chemical-based methods rely on additives like hydroxides and sulfides to induce precipitation of heavy metals. However, these methods often demand high concentrations of chemicals to effectively precipitate heavy metal ions at low concentrations, and the resulting metal precipitates may contain complexing agents (Kurniawan et al. 2006, Qasem et al. 2021). Adsorption-based separation methods, such as the use of granular activated carbon, are commonly employed for the removal of heavy metals. However, most adsorbents lack specificity and the cost of the adsorbent must be carefully considered (Qasem et al. 2021). Ion exchange and reverse osmosis (RO) with selective membrane offer promising avenues for precision separations; However, both ion exchange and RO face challenges and technology gaps. These include a low capacity, poor selectivity against competing ions, especially at high ionic strength, slow uptake and regeneration kinetics, and byproduct residual waste generation (Werber et al. 2016a, Werber et al. 2016b). Understanding the advantages and limitations of diverse water purification methods elucidates the complexities and thus the necessity of trade-offs involved in selecting water purification processes.

* Correspondence author.
E-mail address: junhongchen@uchicago.edu (J. Chen).

https://doi.org/10.1016/j.watres.2024.122665
Received 14 July 2024; Received in revised form 29 September 2024; Accepted 18 October 2024
Available online 21 October 2024

Capacitive deionization (CDI) is a growing technology that provides a low-energy, potentially low-cost option for water purification and treatment (Gamaethiralalage et al. 2021, Suss et al. 2015). When an electrical field is produced between a pair of highly porous electrodes, metal ions can be extracted from wastewater *via* electrosorption (Zhao et al. 2010). When the electrical field is reversed or removed, the adsorbed ions are released into the effluent and the electrodes are regenerated for the next cycle. In the CDI device, electrode materials with a strong adsorption/desorption capacity are critical for the high removal efficiency of metal ions. As a result of their strong mechanical durability, high conductivity, and high specific surface area, carbon materials such as activated carbon (AC) and graphene oxide (GO) have been widely used as CDI electrodes (Li et al. 2010, Wang et al. 2018). To enhance the ion adsorption rate and capacity during the electrosorption process, surface modifications have been developed by mixing carbon electrodes with transition metal nanomaterials, such as ZnO (Kyaw et al. 2020) and MoO_2 (Mao et al. 2020). In addition, the utilization of diverse functional groups to modify GO, including amine (-NH_2), thiol (-SH), halogens, and carboxylic (-COOH) groups, offers a versatile approach to tailor the chemical and physical characteristics of GO. Such modifications have found applications in the adsorption of heavy metals, enhancing the potential for contaminant remediation. In particular, -SH functionalized GO (GO-SH) demonstrated remarkable capability in adsorbing various heavy metals, such as Pb^{2+} (Huang et al. 2019, Pirveysian and Ghiaci 2018), Zn^{2+} (Pirveysian and Ghiaci 2018), and Ni^{2+} (Pirveysian and Ghiaci 2018), owing to its robust chelation affinity towards these contaminants. This significant chelation capability of -SH groups has been employed in the medical use of dimercaprol, a medication containing -SH, in the treatment of toxic exposure to Pb, Hg, Au, and As (Dawn and Whited 2023). On the other hand, GO-COOH and GO-NH_2 have also been proposed as good candidates for the adsorption removal of heavy metals in contaminated water (Yang et al. 2019). However, most reported electrosorption studies for Pb^{2+} removal (Luo et al. 2023, Mao et al. 2020, Pirveysian and Ghiaci 2018) have been conducted in artificial water sources rather than real tap water. The presence of phosphate ions in tap water significantly affects the Pb^{2+} removal performance by CDI (Huang et al. 2019). In addition, there is a notable absence of a comprehensive study on the Pb^{2+} removal efficiency in tap water exhibited by various functional groups as CDI electrode materials, hindering insights into the interfacial adsorption process. Moreover, the coexistence of other cations, particularly Ca^{2+} and Mg^{2+} at elevated concentrations, poses a competitive challenge in Pb^{2+} removal processes. Therefore, there is a critical need to systematically understand and compare the distinct roles of functional groups in Pb^{2+} sorption mechanisms, as well as holistically design CDI devices to achieve selective Pb^{2+} removal against other cations.

In this study, we aim to improve the selectivity and removal efficiency of Pb^{2+} *via* surface modification of CDI electrodes. Through a comprehensive approach combining both computational modeling using density functional theory (DFT) and experimental validation, we systematically explored the impact of distinct functionalized molecular groups (-SH, -COOH, and -NH_2) attached to the electrode surface on the selectivity and removal efficiency of Pb^{2+} in tap water. To comprehensively understand the adsorption behavior of the different electrodes, we employed DFT calculations and X-ray pair distribution function (PDF) analyses to examine the adsorption energy between Pb^{2+} and various functional groups. In addition, the high-angle annular dark-field (HAADF) image demonstrated single-atom adsorption of Pb on the GO-COOH electrode instead of the formation of Pb clusters or particulates. A deep understanding of the mechanism and interactions between different functional groups and lead ions enables us to design a sustainable, adaptable, and reliable prototype CDI platform that is evaluated to function in a wide range of input water qualities for selective and fast separation of target metal species with simultaneous output of clean water.

2. Materials and methods

2.1. Chemicals and materials

All chemicals used in this study were at least American Chemical Society grade. Deionized (DI) water was used to prepare the stock solutions of chemicals. Single-layer graphene oxide (GO) flake was purchased from ACS Material (CA, USA). GO is synthesized using the modified Hummer's method, resulting in an oxidation level of $\geq$95%. Lead chloride ($PbCl_2$, 98%), lead acetate trihydrate ($Pb(Ac)_2$, 99.999%), 3-(mercaptopropyl)trimethoxysilane (MPTMS, 95%), (3-aminopropyl) trimethoxysilane (APTMS, 97%), absolute ethanol (200 proof, anhydrous, $\geq$99.5%), chloroacetic acid (99%), sodium hydroxide (NaOH, $\geq$98%), N-methyl-2-pyrrolidone (NMP), and L-glutathione reduced (GSH, $\geq$98%) were purchased from Sigma-Aldrich (MO, USA). Nitric acid (67–70%) was bought from VWR International LLC (IL, USA). Activated carbon (AC, YP50F) was purchased from Sanwa (Japan). Conductive carbon black and polyvinylidene fluoride (PVDF) binder were bought from MTI Corp (CA, USA). For the CDI tests, tap water with a pH of approximately 7.5 was employed. The measured concentrations of Ca^{2+} and Mg^{2+} in tap water are 37.79 $\pm$ 0.02 ppm and 14.14 $\pm$ 0.04 ppm, respectively.

2.2. Modification of graphene oxide powders with -SH, -NH_2, and -COOH

A total of 400 mg of GO (Fig. S1) was dispersed in 50 mL of concentrated nitric acid and subjected to a 2-hour heating process under constant stirring. Subsequently, the acid-treated GO underwent two rounds of washing using DI water, followed by three rounds of washing with absolute ethanol. The resulting product was then dispersed in 40 mL of absolute ethanol using sonication, resulting in a GO dispersion with a concentration of 10 mg/mL. For the modification of GO with either -SH or -NH_2 functional groups, the same method as previously reported was employed (Huang et al. 2019). Specifically, either MPTMS or APTMS was added to 20 mL of the GO dispersion. The mixture was then heated at 60 °C for 4 hr. The resulting MPTMS-modified GO (named as GO-SH) or ATPMS-modified GO (named as GO-NH_2) was subsequently washed three times with absolute ethanol, Following this, the modified GO was mixed with 0.8 g of activated carbon in 50 mL of ethanol.

On the other hand, the modification of GO with -COOH was carried out following a previously reported method (Chiu et al. 2017, Yu et al. 2015). In detail, 12 g of NaOH was dissolved in 60 mL of water with the help of a water bath sonication. Then, 20 mL of GO suspension at a concentration of 10 mg/mL was introduced into the NaOH solution. 10 g of chloroacetic acid was immediately added to the mixture, and the suspension underwent a 2-hr bath sonication. The resulting GO-COOH was washed 3 times with water, followed by an additional three washes with absolute ethanol. The resulting solids were dispersed in water and subsequently dialyzed in water for at least 3 days. Following this, the dialyzed suspension was mixed with 0.8 g of activated carbon in 50 mL of ethanol.

The three resulting mixtures, namely GO-SH/AC, GO-NH_2/AC, and GO-COOH/AC, were stirred in a fume hood to obtain dried composites. These dried composites were subjected to overnight drying under vacuum conditions at 60 °C. Subsequently, the dried composites were ground until they could pass through a 325-mesh sieve.

2.3. Electrode preparation and characterization

Electrodes were fabricated utilizing a doctor blade method. To prepare the electrode materials, AC, GO-COOH/AC, GO-SH/AC, or GO-NH_2/AC were mixed with carbon black and PVDF binder in a proportion of 72:8:20 (by weight). The mixture was combined in NMP to achieve a consistent and uniform slurry. The resultant slurry was then applied onto a graphite foil using a doctor blade apparatus. Subsequently, the

coated material was subjected to overnight drying under vacuum conditions at 90 °C. The dried material was subsequently cut into 2×2 square inches dimensions, resulting in the production of single-side electrodes (Fig. S2). The mass loading of active materials on the GO electrodes was about 1.0 mg cm^{-2}, with a thickness of about 100 μm.

2.4. Single-pass CDI experimental setup and procedure

In this study, a single-pass mode (Fig. 1f) was employed to investigate the removal of Pb^{2+} from tap water using CDI. The experimental setup consisted of a CDI device connected to a peristaltic pump for controlling the flow rate of Pb^{2+}-containing solutions, while the voltage was regulated by a potentiostat for charging and discharging processes. To improve the removal efficiency and discharge efficiency, anion exchange membranes (AEMs, Fumasep FAS-PET-130) were utilized. In contrast, cation exchange membranes (CEMs) were not used due to potential lead trapping during discharging (Dong et al. 2019). Silicone gaskets were employed to seal the CDI cells at each electrode layer. The charging and discharging voltages applied to the CDI cell were -1.2 V and 1.2 V, respectively, as controlled by a CHI 670E electrochemical workstation (Fig. S3). It is important to note that for cation removal, the working electrode charging voltages were set to be negative by the electrochemical potentiostat. The CDI cell design facilitated radial flux, allowing the flow of water from the bottom center to the four corners of the anodes and ultimately exiting the cell from the top center (Fig. 1g). During the charging process, tap water containing 100 ppb Pb^{2+} was pumped into the CDI cell from a reservoir at a flow rate of 5 mL/min. Notably, to expedite the attainment of the maximum Pb^{2+} removal capacity, the initial concentration of Pb^{2+} used in the CDI test was higher than the EPA's action level for Pb in drinking water (15 ppb) (EPA 2022). To mitigate the re-adsorption of Pb^{2+} during the discharging phase, a higher flow rate of 10 mL/min was utilized to shorten the residence time of Pb^{2+} within the device. To monitor the concentration of cations in the inlet and outlet solutions, samples were collected from both the stock reservoir and the outlet solution. The quantification of cation concentrations was performed using inductively-coupled plasma optical emission spectroscopy (ICP-OES), which allowed for accurate tracking of cations in the solution, aiding in the assessment of the removal efficiency achieved by the CDI process.

2.5. CDI performance

The removal efficiency of each cation at a specific time point (e) and the average removal efficiency ($e_{chg.avg}$) during the charging process were calculated through Eqs. 1 and 2:

$$e = \frac{c_0 - c}{C_0} \times 100\% \quad (1)$$

$$e_{chg.avg} = \frac{c_0 - c_{chg.avg}}{c_0} \times 100\% \quad (2)$$

Here, c represents the mass concentration of the outlet solution at the given sampling time (mg/L), c_0 is the initial mass concentration of

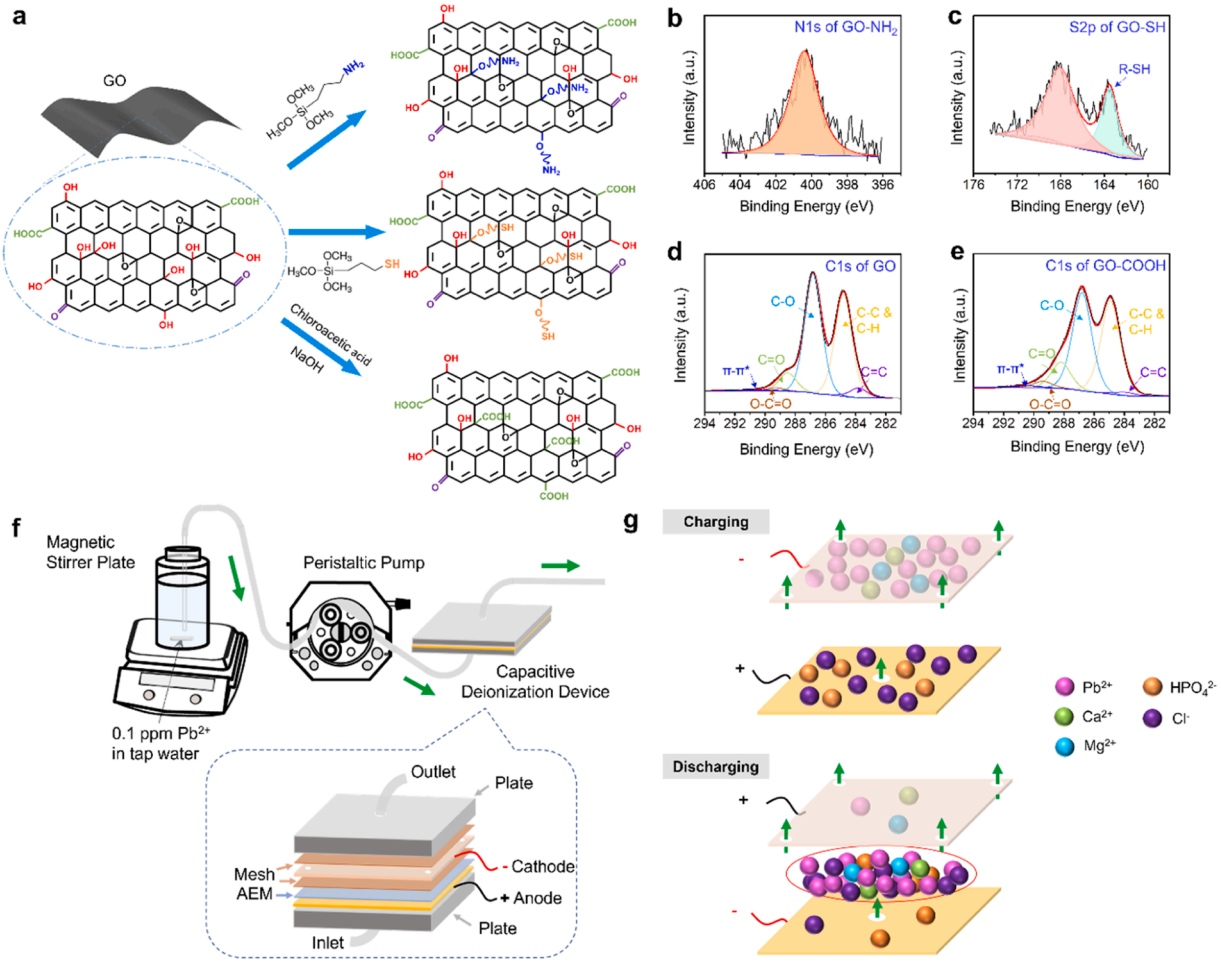

Fig. 1. Surface modification of GO with different functional groups and schematic process for cations removal by a CDI. (a) Schematic representation of the surface modification approaches employed on GO. (b) XPS N1s spectra of GO-NH_2. (c) XPS S2p spectra of GO-SH. (d) XPS C1s spectra of GO. (e) XPS C1s spectra of GO-COOH. (f) Single-pass mode one-layer electrode CDI device prototype. (g) Cations removal mechanism during a charging and discharging cycle.

cations in the stock reservoir (mg/L), and $c_{chg.avg}$ is the mass concentration of cations in the collected outlet solution through the charging process (mg/L).

Furthermore, the selectivity (S) of Pb^{2+} removal was assessed by the relative removal efficiency calculated according to equation (3):

$$S = \frac{e_{chg.avg,\ Pb}}{e_{chg.avg,\ Ca\ or\ Mg}} \times \frac{M_{Ca\ or\ Mg}}{M_{Pb}} \tag{3}$$

Where $e_{avg,\ Pb}$ and $e_{avg,\ Ca\ or\ Mg}$ signify the average removal efficiency of Pb^{2+} and Ca^{2+} or Mg^{2+}, respectively, while M_{Pb} and $M_{Ca\ or\ Mg}$ denote the molar concentrations of Pb^{2+} and Ca^{2+} or Mg^{2+} (mM), respectively. This coefficient quantifies the preferential removal of Pb^{2+} over Ca^{2+} or Mg^{2+} during the charging process.

To assess the stability of Pb removal performance, the cycling CDI test was conducted over 50 cycles, with samples collected at the 5-min time point for every four cycles. Additionally, we calculated several key parameters for Pb removal in tap water, including Pb adsorption capacity (mg g^{-1}, Pb removal mass normalized by the mass of the active materials in the electrodes), Pb adsorption rate (mg g^{-1} min^{-1}), specific energy consumption (SEC) normalized by the mass of Pb removed (J mg^{-1}), charge efficiency (CE, ratio of the charge of adsorbed Pb^{2+} over the total charge supplied to the electrodes), and Pb discharge rate (ratio of desorption over adsorption capacity), and the thermodynamic energy efficiency (TEE, ratio of specific Gibbs free energy of a separation (Δg) over energy consumption (EC) of a CDI process) (Wang et al. 2019), using the following Eqs. 4–11:

$$\text{Pb adsorption capacity} = \left(c_{0,\ Pb} - c_{chg.avg,\ Pb}\right) \times V_{chg.}/m \tag{4}$$

$$\text{Pb adsorption rate} = \text{Pb adsorption capacity}/T \tag{5}$$

$$\text{Specific energy consumption for Pb} = \frac{\int_0^T Uidt}{\left(c_{0,\ Pb} - c_{chg.avg,\ Pb}\right) \times V_{chg.}} \tag{6}$$

$$\text{Charge efficiency for Pb} = \frac{\left(c_{0,\ Pb} - c_{chg.avg,\ Pb}\right) \times V_{chg.} \times z \times F}{M_{Pb} \times 1000 \times \int_0^T idt} \tag{7}$$

$$\text{Pb discharge rate} = \frac{\left(c_{dchg.\ avg,\ Pb} - c_{0,\ Pb}\right) \times V_{dchg.}}{\left(c_{0,\ Pb} - c_{chg.avg,\ Pb}\right) \times V_{chg.}} \times 100\% \tag{8}$$

Where $V_{chg.}$ and $V_{dchg.}$ is the volume of inlet solution during the charging and discharging process (L), respectively, m is the total mass of active materials (AC and GO-based materials) in the electrodes (mg), T is the charging time (min), U is the charging voltage (V), z is the charge of Pb^{2+}, F is the Faraday constant (96,485 C mol^{-1}), M is the molar weight of Pb (207.2 g mol^{-1}), i is the recorded current (A), and $c_{dchg.avg,Pb}$ is the mass concentration of Pb^{2+} in the collected outlet solution through the discharging process (mg/L).

$$TEE = \frac{\Delta g}{EC} \tag{9}$$

$$\Delta g = 2RT\left\{\frac{M_{0,\ Pb}}{\gamma}\ln\left[\frac{M_{0,\ Pb} - \gamma M_{chg.avg,\ Pb}}{M_{0,\ Pb}(1-\gamma)}\right] - M_{chg.avg,\ Pb}\ln\left[\frac{M_{0,\ Pb} - \gamma M_{chg.avg,\ Pb}}{M_{chg.avg,\ Pb}(1-\gamma)}\right]\right. \tag{10}$$

Where, $M_{0,\ Pb}$ is the initial molar concentration of Pb in the stock reservoir, and $M_{chg.avg,\ Pbg}$ is the molar concentration of Pb in the collected outlet solution through the charging process. R is the ideal gas constant (8.3145 J mol^{-1} K^{-1}), and T is the absolute temperature (298 K). EC in Eq. 9 is different from SEC (Eq. 6) as it is not normalized by the mass of Pb removed. Water recovery (γ) is treated water produced relative to the total amount of water processed through the system.

$$\gamma = \frac{V_{charging}}{V_{charging+discharging}} \tag{11}$$

Notably, in our single-pass mode CDI experiments, we used 60 min charging time to evaluate the Pb removal performance in tap water through various electrodes to illustrate the selectivity of the lead separation process. Although all the electrodes demonstrated the ability to function for an extended period beyond 60 min, the Pb adsorption capacity (instead of the overall maximum Pb adsorption capacity) and rate were calculated based on a 60-min charging process.

2.6. Computational modeling

The structural optimization and determination of adsorption energies were conducted through spin-polarized DFT calculations using the Vienna Ab initio Simulation Package (VASP) (Kresse and Furthmüller 1996a, Kresse and Hafner 1993). The calculation employed projector-augmented wave (PAW) (Kresse and Joubert 1999) potentials along with the generalized gradient approximation (GGA) and the Perdew–Burke–Ernzerhof (PBE) (Perdew et al. 1996) exchange-correlation functional. Reciprocal space sampling was performed using a 3×3×1 Monkhorst–Pack k-point mesh for periodic supercells with a k-point density of approximately 36 $Å^{-1}$. The electronic wave functions were expanded in a plane wave basis set with a kinetic energy cutoff of 400 eV for structural optimization. The energy convergence criterion for the electronic wave function was set at 10^{-5} eV. To minimize spurious interactions between the periodic layers, a vacuum layer of approximately 13 Å (periodic length in the z-direction of 20 Å) was selected. The consideration of solvent effects on adsorption energy calculations was incorporated through VASPsol (Mathew et al. 2019b, Mathew et al. 2014a), an implicit solvation model implemented in VASP. The energy cutoff was 800 eV for adsorption energy calculations.

2.7. Characterization of modified GO and visualization of lead presence on the electrode

The functional groups introduced to GO were characterized by X-ray photoelectron spectroscopy (XPS, Thermo Fisher Scientific, USA). The obtained data were analyzed using the Thermo Fisher Avantage Data System to quantify the elemental ratios of GO. The C1s peak (284.8 eV) was employed as the reference peak. To determine the area ratio of C=C, C-C & C-H, C-O, C=O, O=C-OH, and π-π* peaks, the C1s spin-orbit was fitted with C=C (~284 eV), C-C & C-H, (~284.8 eV), C-O (~286.8 eV), C=O (~288.3 eV), O=C-OH (289.3 eV), and π-π* (290.4 eV) by Gauss-Lorentz fitting methods. Additionally, the zeta potential of the GO materials in DI water was measured using a Zetasizer Nano instrument (Malvern Nano ZS). The general morphology and elemental distribution of graphene oxide and the presence of lead on the electrodes were investigated by an analytical transmission electron microscope (TEM) FEI Talos F200X. Single-atom distribution was obtained by using a Thermo Fisher Scientific Spectra 200 equipped with a spherical aberration corrected probe corrector, enabling a HAADF image resolution better than 0.07 nm. Following the charging or discharging processes, the electrodes were carefully taken out and thoroughly cleaned using DI water. A stainless steel blade was used to gently scrape the electrode surface into DI water. Subsequently, a droplet of the dispersion was deposited onto a lacey carbon film coated-Cu grid (01894-F, Ted Pella Inc., CA) for imaging.

2.8. Pb^{2+} adsorption affinity towards -COOH, -NH_2, or -SH in GSH

High energy X-ray experiments were performed at beamline 6-ID-D at the Advanced Photon Source (APS) of Argonne National Laboratory (IL, USA). A collimated monochromatic beam with an area of 0.5 mm^2 and a Varex CT4343 a-Si large area detector were utilized. An incident X-ray energy of 81 keV was chosen, positioned below the Pb K-edge to minimize the X-ray fluorescence effect. The wide angle X-ray scattering data (Q=0.5 to 23 $Å^{-1}$) were analyzed using Fit2D and PDFgetX2

software to correct for dark current, geometrical effects, beam polarization, background, and attenuation. This yielded the total X-ray structure factors S(Q) and corresponding PDF G(r). Samples were run in 2.5 mm diameter silica capillaries (10 μm wall thickness) with concentrations of 1 M Pb acetate in water, and 0.01 M Pb acetate, 0.04 M GSH, and 0.04 M NaOH in water with a pH of 7.5. Notably, due to low signals in the water solution, high concentrations of Pb^{2+} were employed in the measurements. In addition, lead acetate was selected due to its enhanced solubility in water at higher concentrations compared with $PbCl_2$. Experiments were also performed on liquid GSH at a temperature of 480 K.

The empirical potential structure refinement (EPSR) method was employed, which involves a standard Monte Carlo simulation. In this approach, molecules are defined through harmonic force constants between all the atoms, along with angular and dihedral angle constraints. Intermolecular forces are defined by a reference potential comprising Lennard Jones (LJ) potentials and Coulombic terms. Here, the reference LJ potential parameters and partial charges were based on the values taken from Soper, Jorgensen, and Mah (Jorgensen and Swenson 1985, Mah and Jalilehvand 2012, Soper 2007), and were refined in fits to the measured X-ray structure factors of 1 M Pb acetate in water and liquid GSH. The additional empirical potential was added later in the simulation. Once turned on, the empirical potential was determined from the difference between the X-ray diffraction data and the model, perturbing the reference potential. This setup encompassed 5,564 water molecules, 1 Pb acetate molecule, 4 GSH molecules, and 4 NaOH molecules. To establish interactions between Pb^{2+} and -COOH, $-NH_2$, or -SH groups present on the GSH molecule, charges on these groups were artificially increased. Following this initial Monte Carlo equilibration, the Pb ions and the specific functional groups of interest were weakly tethered, and their charges returned to normal values (Table S1). Refinements were made to the empirical potential term to ensure a closer alignment with the X-ray scattering data. Once equilibration was achieved, the constraints were removed.

3. Results and discussion

3.1. Surface modification of GO with different functional groups

In this study, single layer of GO materials were chosen for surface modification with different functional groups. The surface chemistry of graphene oxide is predominantly characterized by hydroxyl (-OH) groups (Fig. 1a) (Guo et al. 2022). To introduce functional groups such as $-NH_2$ and -SH onto GO, a condensation reaction was employed using APTMS and MPTMS, respectively, which contain the silane groups to react with -OH on the GO surface (Abbas et al. 2018). On the other hand, -COOH functionalization was achieved by employing chloroacetic acid to convert -OH groups on the GO surface to -COOH groups (Chiu et al. 2017, Yu et al. 2015). XPS analysis corroborated the successful functionalization: the N1s spectra (Fig. 1b) exhibited characteristic peaks indicating the presence of $-NH_2$ groups, while the S2p spectra (Fig. 1c) confirmed the introduction of -SH groups. Moreover, the evidence of -COOH group incorporation was observed (Fig. 1d,e), where the increasing intensity of the C=O and O-C=O peaks for GO-COOH indicated the successful conversion of -OH groups on the pristine GO surface. Based on the findings from XPS analysis, the elemental ratios of S/C and N/C were determined to be 1.65% and 1.60% respectively. Moreover, the proportion of O-C=O bonds relative to total carbon content escalated from 1.23% in the pristine GO to 2.86% in the GO modified with -COOH groups. This increase signifies a 133% augmentation of -COOH moieties on the GO structure. Therefore, these surface modifications yielded functionalized molecular groups of $-NH_2$, -SH, and -COOH on GO in comparable quantities. The results provide valuable insights into the successful introduction of specific functional groups onto the GO surface, enabling tailored modifications for enhanced adsorption and selective separation applications.

3.2. Comparison of Pb removal performance among different functionalized GO electrodes

The assembled CDI device was employed for the removal of heavy metals from tap water (Fig. 1f). Each pair of cathode and anode in the device constituted one layer. Upon initiation of the charging process, Pb^{2+} accumulated on the cathode surface, subsequently being released at elevated concentrations during discharging (Fig. 1g). To prevent the undesired secondary adsorption of Pb^{2+} on the opposing electrode during discharging, an anion-exchange membrane (AEM, blue color in Fig. 1f) was incorporated, which could enhance the discharging efficiency and retain the selectivity of Pb^{2+} (Dong et al. 2019, Huang et al. 2019). We first explored the effect of the electric force on cation adsorption *via* a single-layer AC electrode. In the absence of the charging process (Fig. 2a), Pb^{2+} removal efficiency dropped to zero after 10 minutes because it reached the maximum surface capacity of physical adsorption in this flow-through experimental system. The lack of an electric force to enhance the cation mobility restricts the adsorption of cations into the depth of the electrode. In addition, almost no adsorption of Ca^{2+} or Mg^{2+} was observed due to the higher affinity of Pb^{2+} compared with Ca^{2+} and Mg^{2+} (Dong et al. 2019, Huang et al. 2019). In contrast, with the charging process, the deployment of a single-layer AC electrode resulted in a Pb^{2+} removal efficiency decline from 47.8% at 3 min of charging to 37.5% at 20 min. This decline can be attributed to the gradual occupation of active adsorption sites near the electrode surface during the charging process. Thus, the electric force is pivotal for effective cation transport, adsorption, and subsequent separation. Notably, the ionic mobility can affect its adsorption efficiency. During the initial charging process, the removal efficiencies of Ca^{2+} and Mg^{2+} exhibited prominence, while that of Pb^{2+} decreased. This phenomenon can be attributed to the higher mobility of Ca^{2+} and Mg^{2+}, enabling them to reach the electrode surface more swiftly than Pb^{2+}. Nonetheless, for subsequent time points, a marked divergence emerged, with Pb^{2+} exhibiting significantly higher removal efficiency than Ca^{2+} and Mg^{2+} because Pb^{2+} has a higher affinity for adsorption compared with Ca^{2+} and Mg^{2+}.

Subsequently, we delved into a comparative assessment of Pb^{2+}, Ca^{2+}, and Mg^{2+} removal efficiency and selectivity in tap water using different electrode configurations, namely by AC, GO-COOH (GO-COOH mixed with AC), GO-SH (GO-SH mixed with AC), and GO-NH_2 (GO-NH_2 mixed with AC). Considering the potential issue of aggregation or stacking arising from a high proportion of GO, which could disrupt the uniformity of the electrode slurry during fabrication and potentially affect Pb adsorption performance, functionalized GO materials were mixed with AC during electrode fabrication. To ensure a clear comparison of removal efficiency differences among the various electrodes, we intentionally restricted the layer count to limit its removal efficiency to some extent. The use of eight layers in the CDI device could potentially result in nearly 100% removal efficiency (Huang et al. 2019), posing challenges in comparing the performance of modified electrodes. In this study, as shown in Fig. S4, we used four layers of AC electrodes, resulting in Pb^{2+} removal efficiencies of 75.7% at 5-min charging and 60.1% after 20-min charging, and gradually declining to 40.2% after 60-min charging (Fig. 2c). Remarkably, compared with the AC electrode, the functionalized GO electrodes mixed with AC exhibited superior and more stable removal efficiencies (Fig. 2d−f). Among the three functionalized GO electrodes, GO-COOH displayed the highest and most stable Pb^{2+} removal efficiency. At 2 min of charging, GO-COOH achieved a Pb^{2+} removal efficiency of 77.7%, maintaining a removal efficiency of 69.2% even after 60 min. In comparison, GO-SH and GO-NH_2 electrodes demonstrated removal efficiencies of 52.2% and 57.3%, respectively, at 60 min of charging. In addition, among all the electrodes, GO-COOH mixed with AC exhibited the highest Pb/Ca and Pb/Mg selectivity (Fig. 2g), achieving values of 2.35×10^4 and 1.60×10^4, respectively. Consequently, GO-COOH mixed with AC displayed the highest Pb^{2+} removal efficiency and selectivity. On the other hand, the

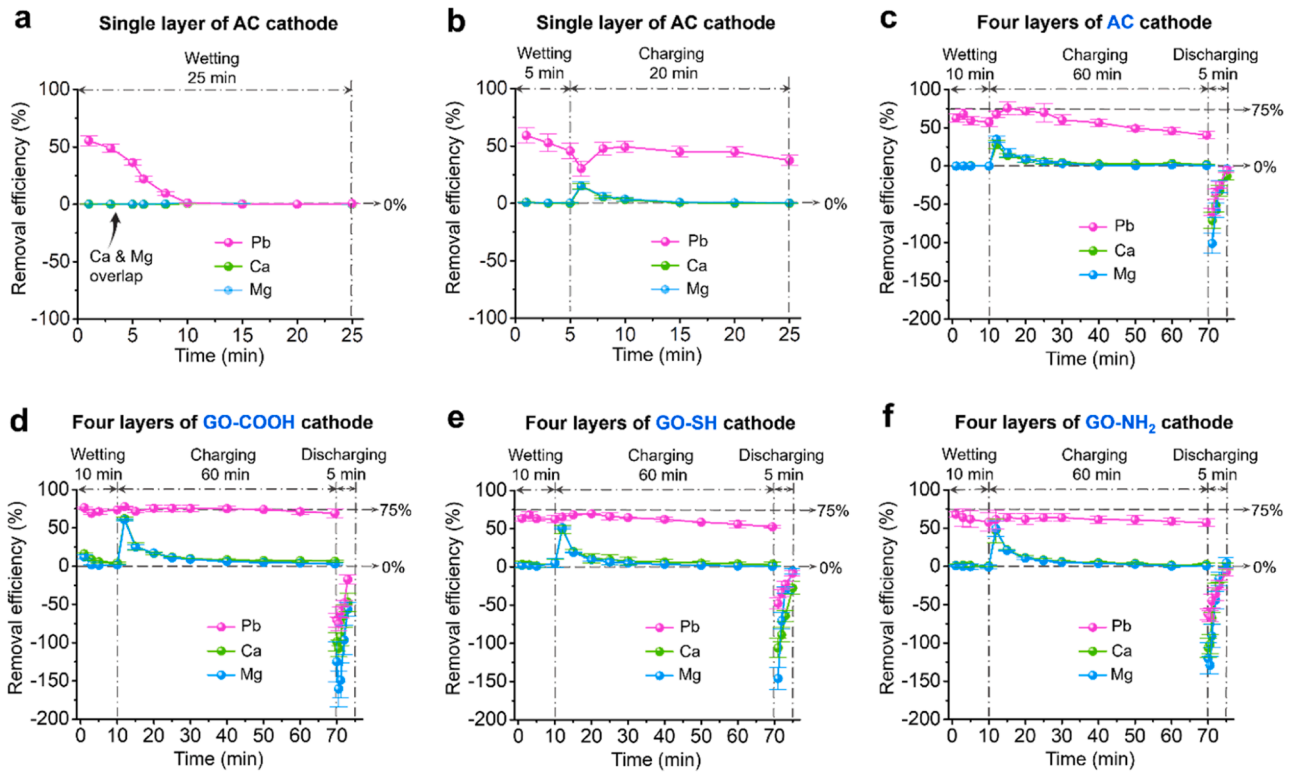

g

Electrodes	Pb/Ca Selectivity	Pb/Mg Selectivity
AC	$(1.50 \pm 0.05) \times 10^4$	$(1.02 \pm 0.04) \times 10^4$
GO-COOH mixed with AC	$(2.35 \pm 0.08) \times 10^4$	$(1.60 \pm 0.05) \times 10^4$
GO-SH mixed with AC	$(2.27 \pm 0.07) \times 10^4$	$(1.22 \pm 0.04) \times 10^4$
GO-NH_2 mixed with AC	$(2.05 \pm 0.06) \times 10^4$	$(1.31 \pm 0.03) \times 10^4$

Fig. 2. Removal efficiencies of Pb^{2+}, Ca^{2+}, and Mg^{2+} by different electrodes and functional groups. (a and b) Removal efficiency of Pb^{2+}, Ca^{2+}, and Mg^{2+} in tap water by a single layer of AC electrode without charging (a) and with charging (b). (c–f) Removal efficiency of Pb^{2+}, Ca^{2+}, and Mg^{2+} by four layers of AC (c), GO-COOH mixed with AC (d), GO-SH mixed with AC (e), and GO-NH_2 mixed with AC (f) electrodes in tap water. (g) Selectivity of Pb^{2+} over Ca^{2+} and Mg^{2+} for different electrodes. Error bars represent the standard deviation from at least duplicate tests.

pH of the inlet solution was about 7.5, while the pH values of the outlet solution ranged from 8.7 to 9.1 during the charging process. The pH difference between the inlet and outlet solutions was attributed to the adsorption of ions on the surfaces of the cathode and anode electrodes.

The selectivity of Pb^{2+} over Ca^{2+} and Mg^{2+} was also investigated for different concentrations (50 ppb, 200 ppb, and 1 ppm) of Pb^{2+} in tap water using GO-COOH electrodes. As shown in Fig. S5, the GO-COOH electrodes exhibited high selectivity for Pb^{2+} across various Pb^{2+} concentrations. We also explored the selectivity of 100 ppb Pb^{2+} over other cations present in tap water, including Na^+, Cu^{2+}, and Fe^{3+}. Our measurements detected about 8.5 ppm of Na^+, 31 ppb of Cu^{2+}, and 24 ppb of Fe^{3+} in tap water. As shown in Table S2, the selectivity of Pb^{2+} over Na^+ was notably high for GO-COOH electrodes, reaching 4.5×10^4. However, GO-COOH electrodes did not show any selectivity of Pb^{2+} over Cu^{2+} and Fe^{3+}, because GO-COOH electrodes exhibited high removal efficiencies for Cu^{2+} and Fe^{3+} during the charging process. During the discharging process, the accumulated cations were swiftly released, resulting in concentrations in the outlet solution much higher than those in the inlet. Thus, at some time point, the removal efficiency values surpassed -100%.

In addition to assessing Pb removal efficiency and selectivity, other parameters were calculated to further evaluate the performance of the CDI device. Fig. S6 displays the cyclic voltammetry (CV) curves of the GO-COOH electrode at various scan rates. The specific capacitance of the GO-COOH electrode was measured to be 97.0 F/g at 10 mV/s. Additionally, electrochemical impedance spectroscopy (EIS) analysis revealed that the GO-COOH electrode exhibited high electrical conductivity and electrochemical performance. For four layers of GO-COOH electrodes, during a 60-min charging process, the total Pb adsorption amount was approximately 0.025 mg, resulting in a Pb adsorption capacity of 0.11 mg g^{-1} (Eq. 4). It is important to note that this value is specific for Pb adsorption rather than all adsorbed cations. Additionally, this value is for Pb adsorption in single-pass mode CDI within 60 min, not representing the maximum Pb adsorption capacity, as the electrodes still exhibited a high Pb removal efficiency at 60 min (Fig. 2d). Accordingly, the Pb adsorption rate was 1.82×10^{-3} mg g^{-1} min^{-1} (Eq. 5). The specific energy consumption (SEC) for Pb was calculated to be 2.5 kJ mg^{-1} (0.69 kWh g^{-1}) (Eq. 6), and the charge efficiency for Pb adsorption was calculated to be 0.04 % (Eq. 7). Furthermore, the Pb discharging rate was about 28.7% (Eq. 8), with the discharging time influencing this value. The water recovery (γ) was calculated to be 85.7% (Eq. 11), and the energy efficiency was 0.005% (Eq. 9). The values of charge efficiency and energy efficiency for Pb were low because the amount of Pb in the tap water was minimal compared with other adsorbed cations. As shown in the current over time profile in Fig. S3, the adsorbed ions were efficiently released within a 3-min discharging period, leading us to adopt a 5-min discharging time in this study. Our previous findings (Huang et al. 2019) indicated that extending the discharging process up to 10 min could increase the Pb discharging rate but at the expense of reduced efficiency. Considering energy consumption, such an extension was unnecessary. Although Pb was only partially removed from the electrode within a short period of

time, it did not significantly impact the long-term cycling performance. To ensure consistent removal performance, CDI systems necessitate electrode materials with high structural stability. Therefore, a cycling CDI test was conducted for the GO-COOH electrodes over 50 cycles, with each cycle consisting of a charge time of 10 min and a discharge time of 2 min. Samples were collected at the 5-min time point for every four cycles. As depicted in Fig. S7, the four layers of GO-COOH electrodes exhibited a consistent and stable Pb^{2+} removal efficiency. XPS characterization was conducted to demonstrate the structural robustness of GO-COOH after Pb^{2+} adsorption/desorption over 50 cycles. As shown in Fig. S8, the percentage of O-C=O bonds relative to all C bonds slightly decreased from 6.54% (fresh GO-COOH electrode) to 5.89% (after 50 cycles), indicating the robust structure of GO-COOH electrodes. Please note that the C1s in Fig. S8 are different from the C1s spectra in Fig. 1d and e that were measured from pure GO-COOH particles instead of the GO-COOH electrode.

3.3. Computational modeling study of metal ion affinity to functional groups

To comprehend the water purification mechanism of the functional groups (-COOH, $-NH_2$, and -SH) at an atomic level, density functional theory calculations were performed using the VASP (Kresse and Furthmüller 1996b, Kresse and Joubert 1999). The adsorption energy (E_{ads}) of three functional groups with the metal ions in water serves as a pertinent descriptor for understanding and comparing their removal efficiency. This is defined by equation (9):

$$E_{ads} = E(FG + ion) - E(FG) - E(ion) \quad (12)$$

where E(FG+ion), E(FG), and E(ion) denote the energy of the functional group adsorbed with the cation, the energy of the functional group itself, and the energy of the cation, respectively. The influence of aqueous solvation was incorporated in the calculations using VASPsol (Mathew et al. 2019a, Mathew et al. 2014b). Furthermore, the pH effect of the solvent and the charge states of the functional groups were taken into account. The acid dissociation constants (pK_a) for -COOH, $-NH_2$, and -SH are approximately 3, 9, and 10, respectively (Danehy and Parameswaran 1968, Vila-Vicosa et al. 2013), while the pH of the tap water solvent is around 7.5. This implies that the dissociation of -COOH to $-COO^-$ and H^+ occurs, as -COOH is deprotonated in the solvent with a pH higher than 3. Conversely, the deprotonation of $-NH_3^+$ to $-NH_2$ and H^+, as well as -SH to $-S^-$ and H^+ are not activated, given that the tap water pH is below 9. Hence, the predominant functional groups in tap water are $-COO^-$ with a negative charge, $-NH_3^+$ with a positive charge, and neutral -SH. To further elucidate the surface charge differences, we measured the zeta potential of the GO materials. As shown in Table S3, among the modified GO materials, GO-COOH exhibited the most negative surface charge of -36.8 ± 2.68 mV, attributed to the deprotonation of -COOH groups into $-COO^-$. GO-SH displayed a surface charge of -26.9 ± 1.13 mV, as the -SH groups remained neutral at neutral pH, showing the surface charge close to that of pristine GO (-28.9 ± 1.42). GO-NH_2 exhibited a less negative charge of -13.05 ± 2.05 mV compared with GO-COOH and GO-SH, as the $-NH_2$ groups are protonated to -NH+ 3 at neutral pH. However, the overall surface charge of GO-NH_2 remained negative due to the presence of other functional groups, such as carboxyl groups, on the surface. Therefore, Pb^{2+}, Ca^{2+}, and Mg^{2+} can directly interact with $-COO^-$ and -SH. However, $-NH_3^+$ repels cations. When metal ions are transported to the electrode surface through electric forces, instead of direct interaction, $-NH_3^+$ initially interacts with a water molecule: $-NH_3^+ + H_2O \rightarrow -NH_2 + H_3O^+$, with the resulting $-NH_2$ adsorbing cations. Therefore, the simulated functional groups are neutral $-NH_2$ and -SH, and charged $-COO^-$. Representative optimized atomic structures of functional groups adsorbed with Pb^{2+} are depicted (Fig. 3 and Fig. S9). In this study, -COOH groups were directly functionalized on the surface of the GO, while $-NH_2$ and -SH groups were introduced using APTMS and MPTMS, respectively, and subsequently linked with GO. Thus, in simulation structures, $-COO^-$ is adsorbed on GO, while $-NH_2$ and -SH are in APTMS and MPTMS molecules, respectively. The charge states of metal ions and functional groups were taken into account in calculations using the counter ion method (Karimadom et al. 2021). In the calculated adsorption energies of functional groups binding with metal ions (Fig. 3e), lower E_{ads} values correspond to stronger adsorption, signifying an enhanced removal efficiency. Notably, for all three functional groups, the E_{ads} values of Pb^{2+} are lower than those of Ca^{2+} and Mg^{2+}. This indicates that all functional groups exhibit a more robust adsorption affinity with Pb^{2+} and a relatively weaker affinity with Ca^{2+} and Mg^{2+}. As a result, all functional groups have the capability to selectively remove Pb^{2+} against Ca^{2+} and Mg^{2+}. Notably, we have taken into account the cathodic polarization effect for cations in the calculation. The effect can be represented as a linear term, q×V, added to the E_{ads}, where q denotes the charge state of the cation and V represents the voltage (George et al. 2023). In investigating the mechanism of cation selectivity, the crucial factor is the difference in E_{ads} between different cations rather than their absolute values. Given that all cations under consideration have the same charge state of +2, the difference in E_{ads} remains consistent regardless of the inclusion of this linear term.

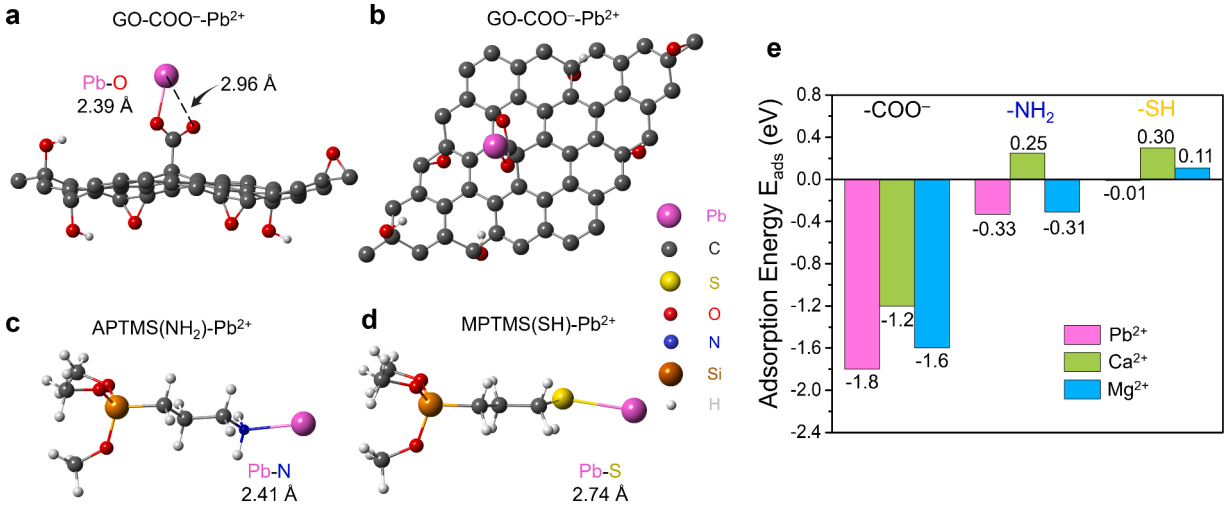

Fig. 3. Optimized atomic structures of functional groups adsorbed with Pb^{2+}. (a and b) Side view (a) and top view (b) of $-COO^-$ on GO adsorbed with Pb^{2+}. (c and d) $-NH_2$ in the APTMS molecule (c) and -SH in the MPTMS molecule (d), both absorbed with Pb^{2+}. (e) The adsorption energies (E_{ads}) between cations and functional groups.

According to the calculations, -COO^- displays the lowest E_{ads} with Pb^{2+} (-1.8 eV) in comparison to -NH_2 (-0.33 eV) and -SH (-0.01 eV). In the interaction between -COO^- and Pb^{2+}, the Pb-O bond has a length of 2.39 Å. Additionally, the other O atom in -COO^- also exhibits a short distance (2.96 Å) to Pb^{2+}, potentially contributing to the adsorption of Pb^{2+} and resulting in its highest affinity to Pb^{2+} among the three functional groups. This observation underscores the superior adsorption and enhanced purification efficiency of -COO^- compared with -NH_2 and -SH. These computational findings align qualitatively with the experimental observations.

3.4. *Binding configuration of Pb^{2+} with GSH*

In both the experimental and modeling results discussed above, the adsorption of Pb^{2+} was individually examined with three distinct functional groups for comparative analysis. To delve deeper into the competitive interactions among these functional groups for Pb^{2+} adsorption, our investigation extended to the binding interactions between Pb^{2+} and GSH—a representative organic molecule incorporating -NH_2, -SH, and -COOH moieties. High-energy synchrotron X-ray experiments were performed at beamline 6-ID-D at the Advanced Photon Source of Argonne National Laboratory, to elucidate the configuration of Pb^{2+} in the presence -COOH, -NH_2, and -SH. As shown in Fig. 4a, the EPSR simulations were configured with a solution containing 0.01 M Pb acetate, 0.04 M GSH, and 0.04 M NaOH in water at pH 7.5 (mimicking tap water pH). Notably, the signals for Pb^{2+} were quite weak in the water, necessitating the use of a high concentration of Pb^{2+} in the measurements. EPSR models are essentially rigid molecule Monte Carlo simulations, with limited flexibility introduced by relaxing constraints for bond angles and dihedral angles. Our simulations contained a total of 5,564 molecules in a cubic box of length 56.2 Å. All molecules were assigned partial charges and initial Lennard-Jones reference potentials (Table S1). While the EPSR model that fits the data does not necessarily give a unique structural 3-dimensional configuration of molecules, they do provide important insights into the types of interactions present in the liquid. Three separate models were constructed to investigate the interactions between Pb and the -COOH, -NH_2, or -SH groups on the GSH molecule as described in the Materials and Methods Section. To achieve a robust correlation between the model and the experimental structure factor, S(Q), an iterative process aimed at minimizing the goodness-of-fit parameter was employed, since a pre-requisite for any realistic model is that it should accurately reproduce the measured data. Extensive data collection was conducted over ensembles comprising approximately 2,000 different atomistic configurations for each chemical group.

By analyzing the Pb-GSH pair distribution functions and configurations (Fig. 4), the average bond distances for Pb interactions with O (-COOH) and S (-SH) were determined to be 2.45 ± 0.10 Å and 2.75 ± 0.07 Å, respectively. This analysis indicates a thermodynamic

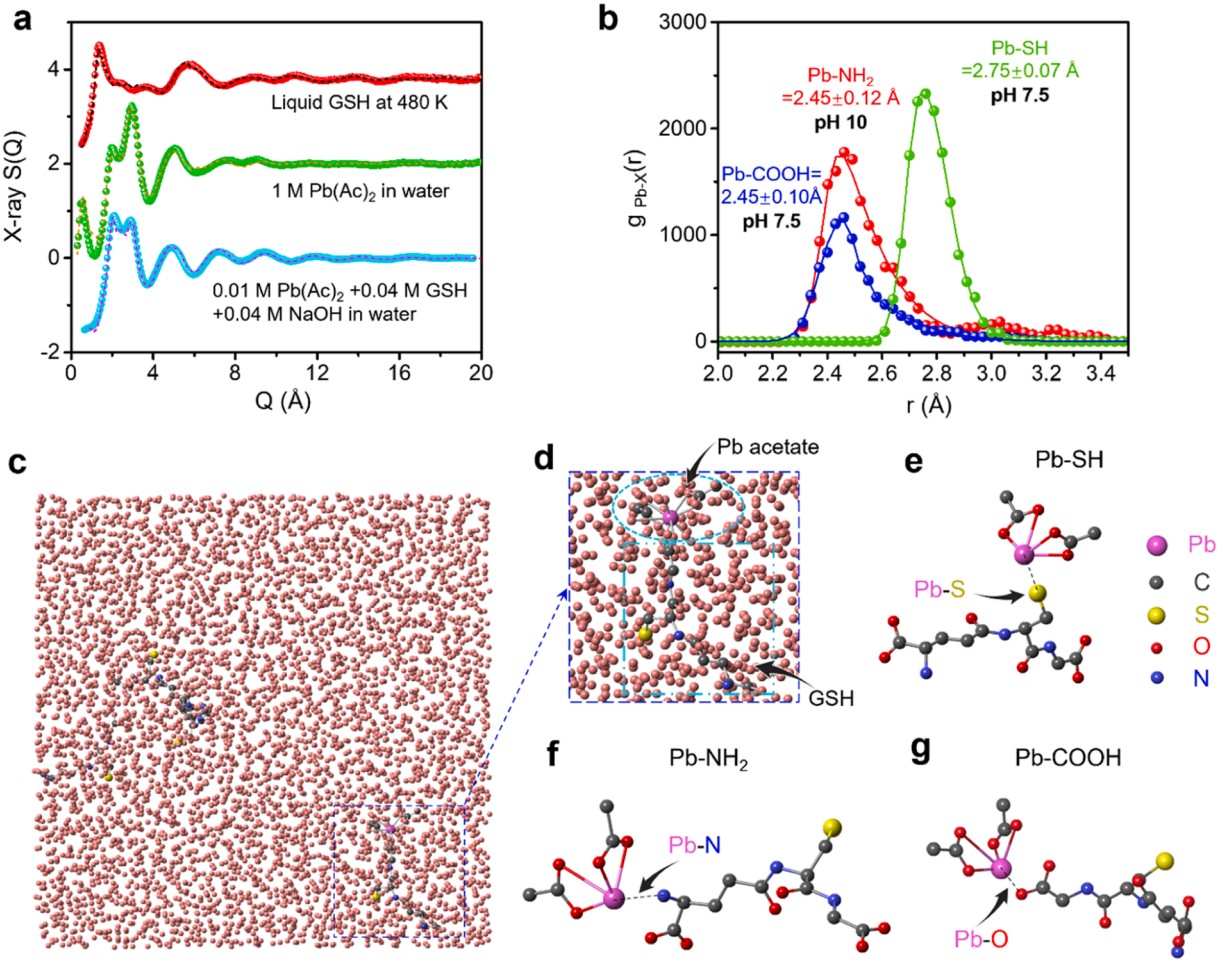

Fig. 4. Binding configuration of Pb^{2+} with GSH. (a) Synchrotron X-ray diffraction data (symbols) and EPSR fits (lines) for liquid GSH at 480K, 1 M Pb acetate in water, and 0.01 M Pb acetate, 0.04 M GSH, and 0.04 M NaOH in water. (b) The Pb-GSH interactions obtained from the EPSR models over ~2,000 configurations. (c and d) A snapshot (c) and its zoomed-in image (d) of one configuration showing the interaction between Pb acetate and GSH. (e-g) Configurations showing the interactions between -SH (e), -NH_2 (f), and -COOH (g) groups in the GSH molecule with Pb acetate taken from the EPSR model. Hydrogens have been omitted for clarity.

preference for Pb to form bonds with -COOH over -SH. It is worth noting that at pH 7.5, -NH_2 exists in the form of -NH_3^+ with a positive charge. Efforts to establish a stable model configuration for Pb-NH_3^+ were deemed unsuccessful when bond distances exceeded 3 Å. In pursuit of a more comprehensive understanding of the Pb and -NH_2 interaction, the solution pH was adjusted to pH 10, effectively neutralizing -NH_2. The ensuing measurement and simulation procedures followed the aforementioned procedure. The resulting average bond distance for the interaction of Pb with N (-NH_2) was determined to be 2.45 ± 0.12 Å, a value akin to that observed for -COOH, indicating that -NH_2 might be a good candidate for Pb adsorption under high pH conditions. The PDF analysis, in agreement with the bond length calculated by DFT (Fig. 3), reinforced the conclusion that in the presence of all three functional groups, Pb exhibits a preference for binding with -COOH at pH 7.5. This insight underscores the intricate interplay between Pb and various functional groups within the GSH molecule and enhances our understanding of the underlying binding mechanisms.

3.5. Single-atom adsorption of Pb on the electrode

To visualize the lead adsorption on the electrodes, we employed high-resolution scanning transmission electron microscopy (STEM) techniques. After the charging process, the cathode electrode was carefully taken out from the CDI device and thoroughly cleaned with DI water. Subsequently, the cathode electrode was delicately scratched by a blade onto a TEM grid for imaging. The resulting scratched GO-COOH electrode exhibits a thin flake morphology (Fig. 5a). The elemental mapping discernibly demonstrated the adsorption of Pb, Ca, and Mg ions onto the surface of the cathode electrode during the charging process (Fig. 5b–f). Notably, certain particle formation containing Ca was observed, possibly calcium carbonate due to the interaction with atmospheric CO_2 during the drying process of the TEM grid. In the context

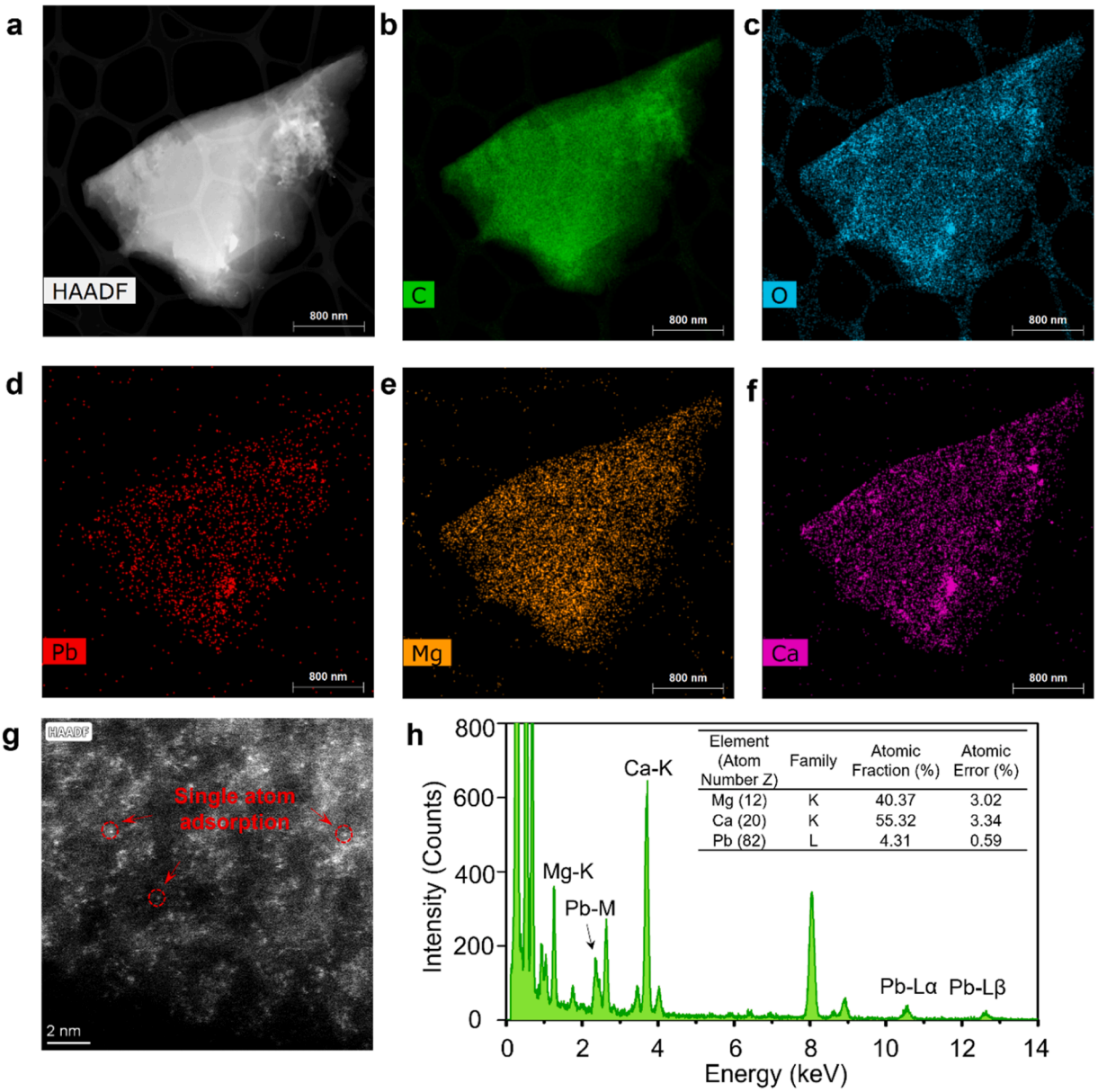

Fig. 5. TEM images of GO-COOH electrode after the charging process. (a) Representative STEM image capturing the morphology of the GO-COOH electrode after the charging process. (b–f) STEM-EDX elemental mapping of C, O, Pb, Mg, and Ca collected from (a). (g) Zoomed-in STEM image, revealing the single atom adsorption of cations on the electrode. (h) EDX spectrum and elemental composition collected from (a). Two TEM grids from duplicated tests were prepared and at least five different spots in each TEM grid were measured.

of phosphate-rich tap water, a conventional notion suggested the formation of Pb^{2+} complexes with phosphate ions, resulting in the creation of $Pb_5(PO_4)_3^+$ species. The complexes may adhere to the cathode electrode surface as particulates or clusters during the charging process (Huang et al. 2019). However, intriguingly, a closer examination through a zoomed-in HAADF image (Fig. 5g) presented an unexpected revelation: the adsorbed Pb was dominantly present as isolated single atoms (~0.3 Å in the red circle), contrasting the initial assumption of nanometer-sized particulates. In the image (Fig. 5g), single atoms appear as bright dots. A cutoff angle larger than 75 mrad was applied during the image capture, such that the HAADF intensity is approximately proportional to the square of atom number (Z^2). Although elements like Pb, Mg, and Ca were all detected from the energy-dispersive X-ray (EDX) spectrum, only single atoms of Pb were dominantly visible as bright dots, owing to the considerably higher atomic number of Pb (Z=82) compared with that of Mg (Z=12) and Ca (Z=20). Moreover, the EDX spectrum (Fig. 5f) indicated the absence of P on the electrode surface, challenging the earlier assumption of phosphate complexation with lead *via* forming clusters or particulates on the electrode surface. Hence, single-atom Pb adsorption occurred on the surface of the GO-COOH electrode. The single-atom adsorption could be attributed to the surface modification of the functional groups on GO, providing isolated sites for interaction with Pb^{2+}. The resulting strong binding between the functional groups and Pb^{2+} stabilized single-atom adsorption and prevented the aggregation of atoms into clusters or nanoparticles. This aspect warrants further detailed investigations for GO-SH and GO-NH_2 electrodes in the future. Theoretically, compared with forming clusters or particulates, single-atom Pb adsorption enables a faster release with a lower energy barrier during the discharging process. As shown in Fig. S10, residual Pb was still observed on the surface of the electrode after the discharging process. This observation aligns with the partial release of Pb observed in the Pb discharging rate (Fig. 2) and was attributed to the relatively short discharging time as previously discussed. However, the observed elemental ratios of adsorbed Ca/Pb and Mg/Pb (Fig. 5f) are approximately 10 and 13, respectively. Considering that the molar concentrations of Ca^{2+} and Mg^{2+} were roughly 2,000 and 1,200 times higher than that of Pb^{2+} in the inlet solution, the results further highlighted the discernible preference of the GO-COOH electrode for selectively adsorbing Pb^{2+} over Ca^{2+} and Mg^{2+}. Collectively, these findings offer an improved understanding of the intricate mechanisms underpinning Pb adsorption within CDI devices.

4. Conclusions

In our investigation, we systematically assessed the influence of distinct functionalized molecular groups (-SH, -COOH, and -NH_2) attached to the GO electrode surface on the selectivity and removal efficiency of Pb^{2+} from tap water using CDI. Surprisingly, our results demonstrate that GO functionalized with -COOH exhibits a significantly higher Pb^{2+} selectivity and removal efficiency compared with -SH and -NH_2. By leveraging DFT calculations and PDF analyses, we have elucidated that Pb^{2+} exhibits a theoretically and experimentally stronger affinity to -COOH functional groups than to -SH and -NH_2. The enhanced understanding of the intricate interactions between various functional groups and Pb^{2+} contributes significantly to the advancement of a versatile CDI platform, facilitating the selective, precise, and expeditious separation of Pb^{2+} for water treatment. In addition, the revealed mechanism of interactions between different functional groups and Pb^{2+} holds promise for applications beyond water treatment, such as in the design of environmental sensors for Pb^{2+} detection. Moreover, although this study primarily focuses on the selective removal of Pb^{2+}, the mechanistic insights uncovered can be applicable to other selective ion removal processes using CDI devices. The platform is also flexible to tune its specificity and can be applied to other non-traditional water sources. This research thus contributes not only to the refinement of the CDI technology but also to the broader field of selective ion separation strategies with potential implications for environmental and analytical advancements. Eq. (12)

CRediT authorship contribution statement

Zhenwei Gao: Writing – review & editing, Writing – original draft, Investigation, Formal analysis, Data curation. **Luqing Wang:** Writing – review & editing, Writing – original draft, Visualization, Investigation, Formal analysis, Data curation. **Xingkang Huang:** Writing – review & editing, Methodology, Investigation, Formal analysis. **Chris Benmore:** Writing – review & editing, Visualization, Resources, Methodology, Investigation. **Haihui Pu:** Writing – review & editing, Methodology, Investigation, Formal analysis. **Jianguo Wen:** Writing – review & editing, Visualization, Methodology, Investigation, Data curation. **Wen Zhuang:** Writing – review & editing, Investigation, Data curation. **Maria K.Y. Chan:** Writing – review & editing, Visualization, Supervision, Software, Methodology, Investigation, Funding acquisition, Data curation. **Junhong Chen:** Writing – review & editing, Supervision, Resources, Project administration, Funding acquisition, Conceptualization.

Declaration of competing interest

The authors declare that they have no known competing financial interests or personal relationships that could have appeared to influence the work reported in this paper.

Acknowledgments

The authors are grateful for the support received from the UChicago Joint Task Force Initiative and the National Science Foundation's Major Research Instrumentation Program (No. 2117896). The authors would like to gratefully acknowledge Dr. Seth B. Darling and Dr. Jeffrey Elam at Argonne National Laboratory for the use of ICP and XPS, and the computing resources provided on Bebop, a high-performance computing cluster operated by the Laboratory Computing Resource Center at Argonne National Laboratory. Work performed at the Center for Nanoscale Materials and Advanced Photon Source (beamline 4-ID-D), both U. S. Department of Energy Office of Science User Facilities, was supported by the U.S. DOE, Office of Basic Energy Sciences, under Contract No. DE-AC02-06CH11357.

Supplementary materials

Supplementary material associated with this article can be found, in the online version, at doi:10.1016/j.watres.2024.122665.

Data availability

Data will be made available on request.

References

Abbas, S.S., Rees, G.J., Kelly, N.L., Dancer, C.E., Hanna, J.V., McNally, T., 2018. Facile silane functionalization of graphene oxide. Nanoscale 10 (34), 16231–16242.
Arbabi, M., Hemati, S., Amiri, M., 2015. Removal of lead ions from industrial wastewater: A review of removal methods. Int. J. Epidemiol. Res 2 (2), 105–109.
Chiu, N.-F., Fan, S.-Y., Yang, C.-D., Huang, T.-Y., 2017. Carboxyl-functionalized graphene oxide composites as SPR biosensors with enhanced sensitivity for immunoaffinity detection. Biosens. Bioelectron 89, 370–376.
Danehy, J.P., Parameswaran, K., 1968. Acidic dissociation constants of thiols. J. Chem. Eng. Data. 13 (3), 386–389.
Dawn, L., Whited, L., 2023. Dimercaprol. StatPearls. StatPearls Publishing, Treasure Island, FL, USA.
Dong, Q., Guo, X., Huang, X., Liu, L., Tallon, R., Taylor, B., Chen, J., 2019. Selective removal of lead ions through capacitive deionization: Role of ion-exchange membrane. Chem. Eng. J. 361, 1535–1542.
EPA, 2022. Ground Water and Drinking Water. Environmental Protection Agency.
Gamaethiralalage, J., Singh, K., Sahin, S., Yoon, J., Elimelech, M., Suss, M., Liang, P., Biesheuvel, P., Zornitta, R.L., De Smet, L., 2021. Recent advances in ion selectivity with capacitive deionization. Energy Environ. Sci. 14 (3), 1095–1120.

George, G., Posada-Pérez, S., Poater, A., Solà, M., 2023. Density functional investigation of the interaction of H_2O with spinel $Li_{1-x}Mn_2O_4$ surfaces: Implications for aqueous Li-ion batteries. Appl. Surf. Sci 612, 155822.
Guo, S., Garaj, S., Bianco, A., Ménard-Moyon, C., 2022. Controlling covalent chemistry on graphene oxide. Nat. Rev. Phys. 4 (4), 247–262.
He, C., Liu, Z., Wu, J., Pan, X., Fang, Z., Li, J., Bryan, B.A., 2021. Future global urban water scarcity and potential solutions. Nat. Commun. 12 (1), 4667.
Huang, X., Guo, X., Dong, Q., Liu, L., Tallon, R., Chen, J., 2019. Zero-wastewater capacitive deionization: selective removal of heavy metal ions in tap water assisted by phosphate ions. Environ. Sci. Nano 6 (11), 3225–3231.
Jorgensen, W.L., Swenson, C.J., 1985. Optimized intermolecular potential functions for amides and peptides. Structure and properties of liquid amides. J. Am. Chem. Soc. 107 (3), 569–578.
Karimadom, B.R., Meyerstein, D., Kornweitz, H., 2021. Calculating the adsorption energy of a charged adsorbent in a periodic metallic system – the case of BH_4^- hydrolysis on the Ag(111) surface. Phys. Chem. Chem. Phys. 23 (45), 25667–25678.
Kresse, G., Furthmüller, J., 1996a. Efficient iterative schemes for ab initio total-energy calculations using a plane-wave basis set. Phys. Rev. B 54 (16), 11169–11186.
Kresse, G., Furthmüller, J., 1996b. Efficient iterative schemes for ab initio total-energy calculations using a plane-wave basis set. Phys. Rev. B 54 (16), 11169.
Kresse, G., Hafner, J., 1993. Ab initio molecular dynamics for liquid metals. Phys. Rev. B 47 (1), 558–561.
Kresse, G., Joubert, D., 1999. From ultrasoft pseudopotentials to the projector augmented-wave method. Phys. Rev. B 59 (3), 1758.
Kurniawan, T.A., Chan, G.Y., Lo, W.-H., Babel, S., 2006. Physico–chemical treatment techniques for wastewater laden with heavy metals. Chem. Eng. J. 118 (1-2), 83–98.
Kyaw, H.H., Myint, M.T.Z., Al-Harthi, S., Al-Abri, M., 2020. Removal of heavy metal ions by capacitive deionization: Effect of surface modification on ions adsorption. J. Hazard. Mater. 385, 121565.
Li, H., Zou, L., Pan, L., Sun, Z., 2010. Novel graphene-like electrodes for capacitive deionization. Environ. Sci. Technol. 44 (22), 8692–8697.
Luo, J., Mu, J., Li, X., Liu, B., 2023. High Capacitive Removal of Pb^{2+} from Wastewater and Mechanism Study over MoO_2@N-Doped Hollow Carbon Sphere Anodes. ACS ES&T Water 3 (2), 429–437.
Mah, V., Jalilehvand, F., 2012. Lead(II) complex formation with glutathione. Inorg. Chem. 51 (11), 6285–6298.
Mao, M., Yan, T., Chen, G., Zhang, J., Shi, L., Zhang, D., 2020. Selective capacitive removal of Pb^{2+} from wastewater over redox-active electrodes. Environ. Sci. Technol. 55 (1), 730–737.
Mathew, K., Kolluru, V., Mula, S., Steinmann, S.N., Hennig, R.G., 2019a. Implicit self-consistent electrolyte model in plane-wave density-functional theory. J. Chem. Phys. 151 (23).
Mathew, K., Kolluru, V.C., Mula, S., Steinmann, S.N., Hennig, R.G., 2019b. Implicit self-consistent electrolyte model in plane-wave density-functional theory. J. Chem. Phys. 151 (23), 234101.
Mathew, K., Sundararaman, R., Letchworth-Weaver, K., Arias, T., Hennig, R.G., 2014a. Implicit solvation model for density-functional study of nanocrystal surfaces and reaction pathways. J. Chem. Phys. 140 (8), 084106.
Mathew, K., Sundararaman, R., Letchworth-Weaver, K., Arias, T., Hennig, R.G., 2014b. Implicit solvation model for density-functional study of nanocrystal surfaces and reaction pathways. J. Chem. Phys. 140 (8).
Navas-Acien, A., Guallar, E., Silbergeld, E.K., Rothenberg, S.J., 2007. Lead exposure and cardiovascular disease—a systematic review. Environ. Health Perspect. 115 (3), 472–482.
Perdew, J.P., Burke, K., Ernzerhof, M., 1996. Generalized gradient approximation made simple. Phys. Rev. Lett. 77 (18), 3865.
Pirveysian, M., Ghiaci, M., 2018. Synthesis and characterization of sulfur functionalized graphene oxide nanosheets as efficient sorbent for removal of Pb^{2+}, Cd^{2+}, Ni^{2+} and Zn^{2+} ions from aqueous solution: A combined thermodynamic and kinetic studies. Appl. Surf. Sci. 428, 98–109.
Qasem, N.A., Mohammed, R.H., Lawal, D.U., 2021. Removal of heavy metal ions from wastewater: A comprehensive and critical review. npj Clean Water 4 (1), 36.
Soper, A., 2007. Joint structure refinement of x-ray and neutron diffraction data on disordered materials: application to liquid water. J. Phys.: Condens. Matter 19 (33), 335206.
Suss, M.E., Porada, S., Sun, X., Biesheuvel, P.M., Yoon, J., Presser, V., 2015. Water desalination via capacitive deionization: what is it and what can we expect from it? Energy Environ. Sci. 8 (8), 2296–2319.
Vila-Vicosa, D., Teixeira, V.H., Santos, H.A., Machuqueiro, M., 2013. Conformational study of GSH and GSSG using constant-pH molecular dynamics simulations. J. Phys. Chem. B 117 (25), 7507–7517.
Wang, L., Dykstra, J., Lin, S., 2019. Energy efficiency of capacitive deionization. Environ. Sci. Technol. 53 (7), 3366–3378.
Wang, S., Li, X., Zhao, H., Quan, X., Chen, S., Yu, H., 2018. Enhanced adsorption of ionizable antibiotics on activated carbon fiber under electrochemical assistance in continuous-flow modes. Water Res 134, 162–169.
Wei, R., Chen, C., Kou, M., Liu, Z., Wang, Z., Cai, J., Tan, W., 2023. Heavy metal concentrations in rice that meet safety standards can still pose a risk to human health. Commun. Earth Environ. 4 (1), 84.
Werber, J.R., Deshmukh, A., Elimelech, M., 2016a. The critical need for increased selectivity, not increased water permeability, for desalination membranes. Environ. Sci. Technol. Lett. 3 (4), 112–120.
Werber, J.R., Osuji, C.O., Elimelech, M., 2016b. Materials for next-generation desalination and water purification membranes. Nat. Rev. Mater. 1 (5), 1–15.
WHO, 2005. Nutrients in drinking water. World Health Organization.
Yang, X., Wan, Y., Zheng, Y., He, F., Yu, Z., Huang, J., Wang, H., Ok, Y.S., Jiang, Y., Gao, B., 2019. Surface functional groups of carbon-based adsorbents and their roles in the removal of heavy metals from aqueous solutions: a critical review. Chem. Eng. J. 366, 608–621.
Yu, S., Liu, J., Zhu, W., Hu, Z.-T., Lim, T.-T., Yan, X., 2015. Facile room-temperature synthesis of carboxylated graphene oxide-copper sulfide nanocomposite with high photodegradation and disinfection activities under solar light irradiation. Sci. Rep. 5 (1), 16369.
Zhao, R., Biesheuvel, P., Miedema, H., Bruning, H., Van der Wal, A., 2010. Charge efficiency: a functional tool to probe the double-layer structure inside of porous electrodes and application in the modeling of capacitive deionization. J. Phys. Chem. Lett. 1 (1), 205–210.